Natural Glycyrrhizic Acid-Tailored Nanoparticles Toward the Enhancement of Pesticide Bioavailability

Kailun Wei, Zilu Li, Zhiran Zheng, Yuxia Gao, Qiliang Huang, Min-Hui Li, Jun Hu

Natural Glycyrrhizic Acid-Tailored Nanoparticles Toward the Enhancement of Pesticide Bioavailability

Kailun Wei, Zilu Li, Zhiran Zheng, Yuxia Gao, Qiliang Huang, Min-Hui Li, and Jun Hu**

K. Wei, Z. Zheng, J. Hu
Beijing Advanced Innovation Center for Soft Matter Science and Engineering, Beijing University of Chemical Technology, North Third Ring Road 15, Chaoyang District, Beijing 100029, China
E-mail: jhu@mail.buct.edu.cn

Z. Li, Y. Gao
Department of Applied Chemistry, College of Science, China Agricultural University, Yuanmingyuan West Road 2, Haidian District, Beijing 100193, China
E-mail: gaoyuxia@cau.edu.cn

Q. Huang,
State Key Laboratory for Biology of Plant Diseases and Insect Pests, Institute of Plant Protection, Chinese Academy of Agricultural Sciences, Yuanmingyuan West Road 2, Haidian District, Beijing 100193, China

M.-H. Li
Chimie ParisTech, PSL University, CNRS, Institut de Recherche de Chimie Paris, 11 rue Pierre et Marie Curie, Paris 75005, France

Keywords: nanoparticle, co-assembly, deposition, controlled-release, glycyrrhizic acid

Pesticide spraying serves as a prevalent segment in crop production for substantial economic and ecological benefits. Nevertheless, the existing pesticide formulations are often plagued by

droplets rebounding during spraying process, and the controlled-release, photolysis protection, and non-targeted bio-friendliness are not inadequately considered. Herein, by combining spinosad (SSD, a model pesticide) with glycyrrhizic acid (GL) as an attractive building block, we have employed a supramolecular co-assembly strategy to elaborate pesticide formulations (GL-SSD) simultaneously featuring high deposition, controlled-release, and environmental friendliness. The resulting spherical GL-SSD nanoparticles (NPs) have an average diameter of 207 nm and show an improved 5.2-fold photostability compared with commercial spinosad suspension (SSD SC). Upon impacting on hydrophobic surfaces of polytetrafluoroethylene film and cabbage leaf, the droplets of GL-SSD NPs exhibit superior affinity to the micro/nano structure of the surface. Consequently, the droplet rebounding is inhibited effectively, ensuring high deposition efficiency of droplets on surfaces. In addition, the release of SSD from GL-SSD NPs can be controlled by pH variation. Indoor toxicity and pot experiments demonstrate that GL-SSD NPs possess good control efficacy against *Plutella xylostella*. Our work offers an alternative approach for the development of multi-functional and sustainable pesticide formulations with promising potentials in actual agriculture production.

1. Introduction

Utilization of pesticides in agriculture effectively safeguards crops against weeds, insects, and diseases, and plays a prominent role in enhancing crop yield and quality.[1,2] Due to the low surface free energy and divergent nano/micro-roughness, most crop leaves are hydrophobic or even superhydrophobic, which often cause unacceptable droplet rebounding/splashing during foliar spraying.[3-5] Meanwhile, the controlled-release, photolysis protection, and non-targeted bio-friendliness are not inadequately considered for the majority of pesticides. Consequently, the excessive usage of pesticides poses a grievous threat to ecosystems and human health.[6-9] Two strategies are currently employed to improve the utilization efficiency of pesticides. The first strategy incorporates additives like surfactants,[10,11] polymers,[12,13] and aggregates[14-16] to mitigate droplets bouncing, breaking, and splashing on leaves. During the impact process, surfactants with fast diffusion rate can reduce the surface tension and promote droplet spreading, polymers would dissipate impact kinetic energy by means of extensional viscosity for restraining droplet rebound, while aggregates are able to reinforce interactions between

droplets and surface micro/nanostructures to delay droplet retraction.[17,18] The second strategy involves the fabrication of functional nanocarriers for pesticides using polymer-, silica-, and carbon-based materials.[19-24] By taking advantages of small size, large surface area, and smart responses, these nanocarriers not only enhance the dispersibility and stability of pesticides, but also facilitate target deposition and dose transfer. Nevertheless, the former strategy only focuses on droplet deposition process, while neglecting encapsulation and controlled-release of pesticides. The elaboration of nanocarriers in the second strategy always requires sophisticated synthesis procedures and are consequently expensive.[25-27] Both of these existing strategies for controlling pesticide losses still fail to work in two or more aspects in all application stages of pesticides. Therefore, the development of pesticide formulations that simultaneously possess high deposition, controlled-release, and environmental friendliness remains a challenge.

Supramolecular assembly provides a potential solution to take up the above challenge. Driven by non-covalent interactions, some specific molecules are able to spontaneously assemble in aqueous solutions to form diverse nanostructures with dynamic reversibility, morphological variability, and stimuli-responsiveness.[28-32] The design of pesticide formulations by supramolecular assembly present therefore three merits: 1) the water-based preparation process is simple, and avoids tedious chemical synthesis, which fulfills the requirement of sustainable agriculture; 2) compared to pesticide technical and mixtures, pesticide-tailored assemblies possess distinctive physicochemical properties to strengthen interactions with surface micro/nanostructures, which results in superb affinity to leaf surfaces during the droplet impact process; and 3) pesticide-tailored assemblies can precisely release pesticides in a controllable manner under different stimuli because of dynamic reversible non-covalent interactions.[33-35] Inspired by these unique features, here we developed a pesticide formulation to comprehensively enhance the utilization efficiency of pesticides in terms of encapsulation, deposition, and release (**Scheme 1**). In this formulation, glycyrrhizic acid (GL) and spinosad (SSD) were taken as the assembly building block and model pesticide, respectively.

As a natural occurring triterpenoid saponin in licorice root,[36] GL has an intrinsic

amphiphilic structure consisted by a hydrophobic triterpenoid and a hydrophilic diglucuronic unit, which makes GL a natural biocompatible surfactant.[37,38] The presence of multiple hydroxyl and carboxyl groups in GL, together with the rigid skeleton, facilitates the synergistic regulation of hydrogen bonding, van der Waals force, and electrostatic attraction in assemblies.[39,40] As for SSD, it is a highly effective macrolide biorational pesticide to manage cotton bollworms, tobacco budworms, vegetable diamondback moths, and thrips by activating nicotinic acetylcholine receptors. Its tertiary amine group renders SSD susceptible to protonation in acidic condition.[41,42] Benefiting from the amphiphilicity of GL and its non-covalent bonding with SSD, the GL-tailored SSD nanoparticles (GL-SSD NPs) can be easily obtained by mixing GL and SSD in aqueous solution. The resultant GL-SSD NPs are spherical particles with a mean diameter of 207 nm, and possess an improved 5.2-fold photostability compared with commercial spinosad suspension (SSD SC). Upon spraying on hydrophobic surfaces, the droplets of GL-SSD NPs exhibit superior affinity to the micro/nano structure of the surface. As a result, the droplet rebounding is inhibited and the deposition on surface is improved efficiently. Because of the dynamic nature of GL-SSD NPs, SSD can be released in a controllable manner by changing pH value. Indoor toxicity and pot experiments indicated that GL-SSD NPs own higher insecticidal activity than SSD SC. This supramolecular assembly strategy is simple and efficient, providing a feasible way to develop pesticide formulations with multi-functionality and sustainability.

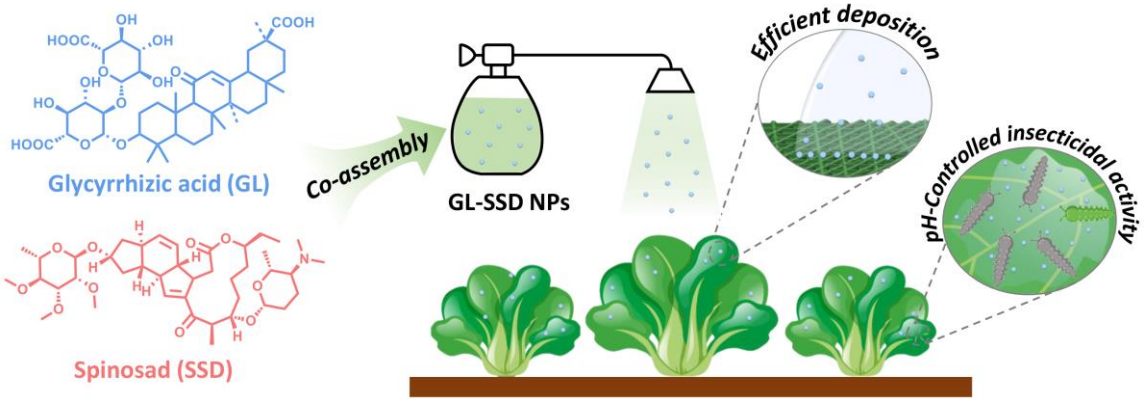

Scheme 1. Schematic illustration for the elaboration of GL-SSD NPs co-assembled from glycyrrhizic acid (GL) and spinosad (SSD), and its performance in deposition, controlled release, and insecticidal activity.

2. Results and discussion

2.1 Interfacial performance of GL

Prior to the co-assembly of GL and SSD, the interfacial behavior of GL in water-toluene was investigated using pendant drop tensiometry. As shown in **Figure 1**a and **Video S1** (Supporting Information), when the droplets of GL aqueous solution immersed in toluene at a concentration of 0.03, 0.05, 0.10, and 0.15 mM were extracted, the interfacial area diminished and appeared visible wrinkling on droplet interface at 51, 41, 26, and 18 s, respectively. Similarly, when the droplets were fully siphoned into the needle and reinjected to initial volume, the wrinkling phenomenon was resurfaced, along with the gradual expand of droplet from irregular to inerratic. Notably, that droplet wrinkling was exclusively observed in the concentration range of 0.03-0.25 mM, while no interfacial jamming emerged in GL droplets below 0.03 mM or above 0.25 mM (Figure S1, Supporting Information). The appearance of wrinkling in the extraction-reinjection process strongly revealed the formation of elastic film at water-toluene interface with certain mechanical robustness. The reason behind this interface jamming may be the failure of GL molecules to migrate from interface to bulk phase when interfacial surface area of droplets decreased. To substantiate this conjecture, the time-resolved interfacial tension (IFT) between GL solution and toluene were measured. When the concentration of GL was lower than 0.03 mM, the interfacial tension between toluene and GL solutions was approximately equivalent to that between pure water and toluene (~32 mN/m). As the concentration of GL solution increased from 0.03 to 0.25 mM, the interfacial tension declined to 6.8 mN/m, while retaining invariable at 6.8 mN/m from 0.25 to 1.00 mM (Figure 1b). Accordingly, 0.25 mM was determined to be the critical micelle concentration (CMC) of GL molecules at water-toluene interface (Figure 1c). This meant that droplet shrinkage experienced below CMC of GL, different from the droplet wrinkling above CMC in other reported works.[43,44] To further explain this phenomenon, the interfacial adsorption capacity and cross-sectional area of GL molecules at different concentrations were calculated. The interfacial adsorption capacity of GL increased proportionally with the concentration, reaching a maximum value of 11.48×10^{-3} mol/m^2 at 0.25 mM. Conversely, the cross-sectional area decreased as the concentration rose with a minimum value of 0.14 nm^2 (Figure

1d and Table S1, Supporting Information). On the basis of the aforementioned results, a possible arrangement model of GL molecules at water-toluene interface was predicted (Figure S2, Supporting Information). At the concentration less than 0.03 mM, GL molecules were insufficient to stack into a film at water-toluene interface upon extracting. When the concentration of GL ranged from 0.03 to 0.25 mM, an increase in molecule numbers at the interface led to the enhanced intermolecular interactions of the nicely packed neighboring molecules, consequently forming an interface film with optimal toughness and strength. During the extraction process, the migration of GL molecules from interface to bulk phase was too slow, resulting in interface jamming and appearing wrinkled film. Once the concentration exceeded 0.25 mM, the quantity of GL molecules at the interface attained saturation. As a result, the molecules were almost upright at the interface due to the limited cross-sectional area, making them difficult to undergo conformational adjustment and rearrangements to form an interfacial film. To sum up, GL was an extraordinary amphiphilic molecule that can generate interfacial film at oil-water interface.

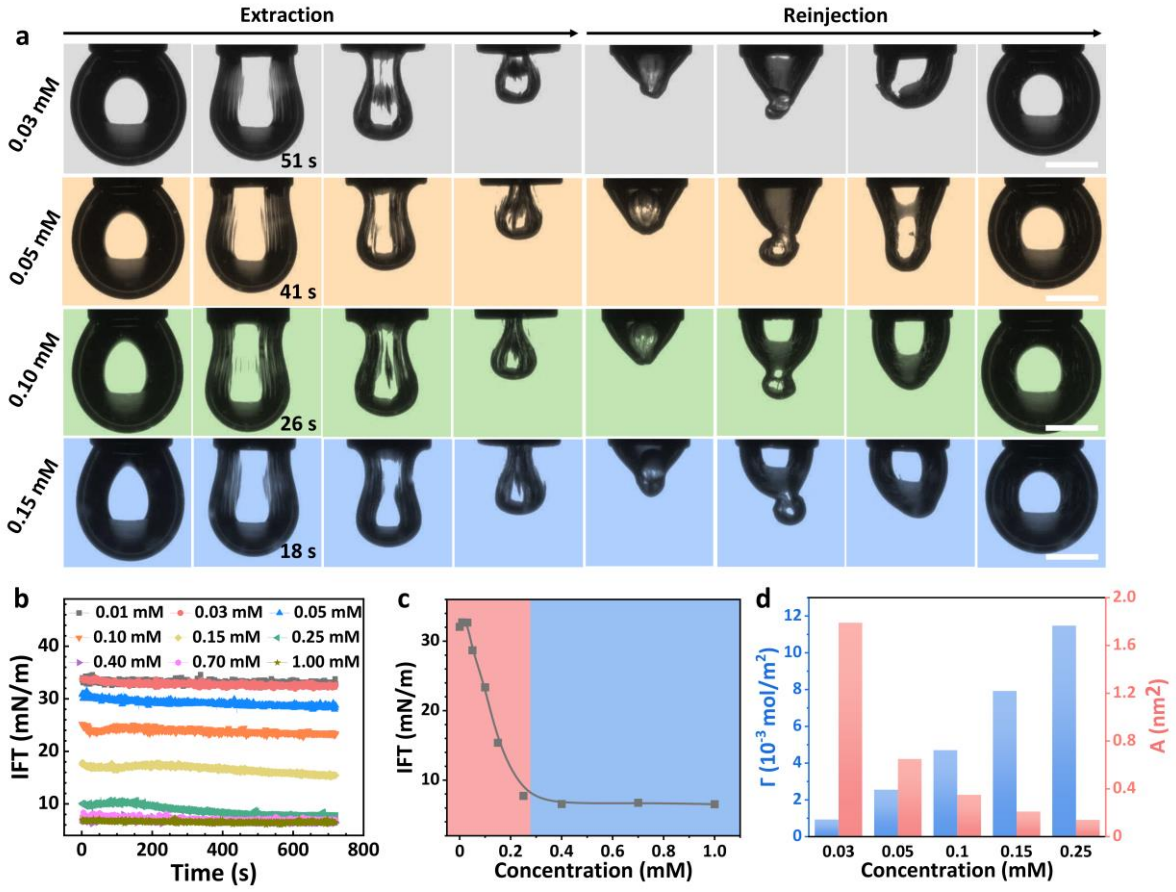

Figure 1. Interfacial performance of GL. a) Photographs capturing the shape evolutions of

pendant droplets with GL concentrations of 0.03, 0.05, 0.10, and 0.15 mM at water-toluene interfaces during the extraction-reinjection process. Scale bar is 1 mm. b) Time- and c) concentration-dependent toluene-water interfacial tension (IFT) of GL molecules. d) Interfacial adsorption capacity and cross-sectional area of GL molecules at water-toluene interface under different concentrations.

2.2 Co-assembly and characterization of GL-SSD NPs

Initially, SSD with low water solubility was dissolved into methanol to form a clear solution, which then was continuously dropped into an aqueous solution of GL under ultrasonic conditions. Since the GL solution was acidic, the tertiary amine group in SSD was easily protonated into quaternary ammonium bearing positive charges. As a result, the amphiphilic GL spontaneously interacted with the protonated SSD to afford stable spherical co-assemblies of GL-SSD NPs. The resulting GL-SSD NPs exhibited a pronounced Tyndall phenomenon (**Figure 2**a), where the diameter, polydispersity index (PDI), and zeta potential of GL-SSD NPs measured by dynamic light scattering (DLS) were 272 nm, 0.469, and -31 mV, respectively. Transmission electron microscope (TEM) images further revealed that GL-SSD NPs were spherical particles with an average diameter of 207 nm (Figure 2b and S3a, Supporting Information), while neat GL would assemble into nanoparticles with a diameter approximately 30 nm (Figure 2c and S3b, Supporting Information). Thermal gravimetric analysis (TGA) was conducted to detect the thermal stability of GL-SSD NPs (Figure S4, Supporting Information). For neat SSD and GL, both of them implied a distinct diminishing region of weight, where SSD degraded from 260 to 430℃ while GL was pyrolyzed from 160 to 500℃. On the contrary, GL-SSD NPs mainly displayed two evident regions of mass loss. The first weight loss (26%) from 160 to 260℃ was assigned to the degradation of GL, and the second weight loss (61%) between 260 and 500℃ was attributed to the thermal decomposition of both GL and SSD, revealing good thermal stability of GL-SSD NPs.

To elucidate non-covalent interactions involved in the co-assembly of GL and SSD, Fourier transform infrared spectrometer (FTIR) of SSD, GL, and GL-SSD NPs were studied (Figure 2d and 2e). The peaks at 1708 and 1068 cm^{-1} of SSD were ascribed to the stretching vibration of ester carbonyl (O-C=O) and tertiary amine (-$N(CH_3)_2$) group, while the peaks located at

3439 and 1728 cm^{-1} were attributed to the stretching vibration of hydroxyl (-OH) and carboxyl (C=O) group of GL. On the contrary, the peak of -$N(CH_3)_2$ on SSD shifted from 1068 to 1060 cm^{-1}, and the peak of carboxylate (COO^-) group appeared at 1604 and 1454 cm^{-1} in GL-SSD NPs, indicative of the existence of electrostatic attraction between the protonated amine group in SSD and carboxyl groups in GL.[45] Moreover, the peak of ester carbonyl group on SSD shifted from 1708 cm^{-1} to a higher wavenumber of 1722 cm^{-1} in GL-SSD NPs, along with the shift of hydroxyl group in GL from 3439 to 3384 cm^{-1}, which were ascribed to hydrogen bonding between SSD and GL. Apparently, the synergistic interplay of hydrogen bonding and electrostatic force between GL and SSD promoted the formation of GL-SSD NPs.

Molecular dynamics (MD) simulations were executed to further analyze the co-assembly behavior of GL and SSD. As depicted in Figure 2f and S5 (Supporting Information), SSD and GL with water molecules were randomly distributed in simulated boxes with dimensions of 8 × 8 × 8 nm^3, and after 100 ns they forged into stable co-assemblies. During this process, the root mean square deviation (RMSD) fractionally undulated with a final value of 2.65 ± 0.10 nm (Figure S6a, Supporting Information), and the solvent accessible surface area (SASA) visibly cut down in the initial stage and subsequently attained a stable state after 100 ns with an average value of 159.69 ± 5.40 nm^2 (Figure S6b, Supporting Information). These results manifested that GL and SSD tended to be stable after 100 ns and preferred to form more compact co-assemblies by reducing the exposure of molecules to water solvents. In addition, statistical analysis of the driving forces behind the co-assembly was conducted. The hydrogen bond number was 13.15 ± 3.40 (Figure S6c, Supporting Information), while binding energy of electrostatic attraction and van der Waals force were −514.19 ± 46.72 and −5241.58 ± 107.19 kJ mol^{-1}, respectively (Figure S6d, Supporting Information), testifying the hydrogen bonding, van der Waals force, and electrostatic attraction were the principal driving forces, consistent with FTIR results. By systematically analyzing the conformation of GL and SSD using MD simulation, a schematic diagram showing molecular interactions was illustrated in Figure 2g.

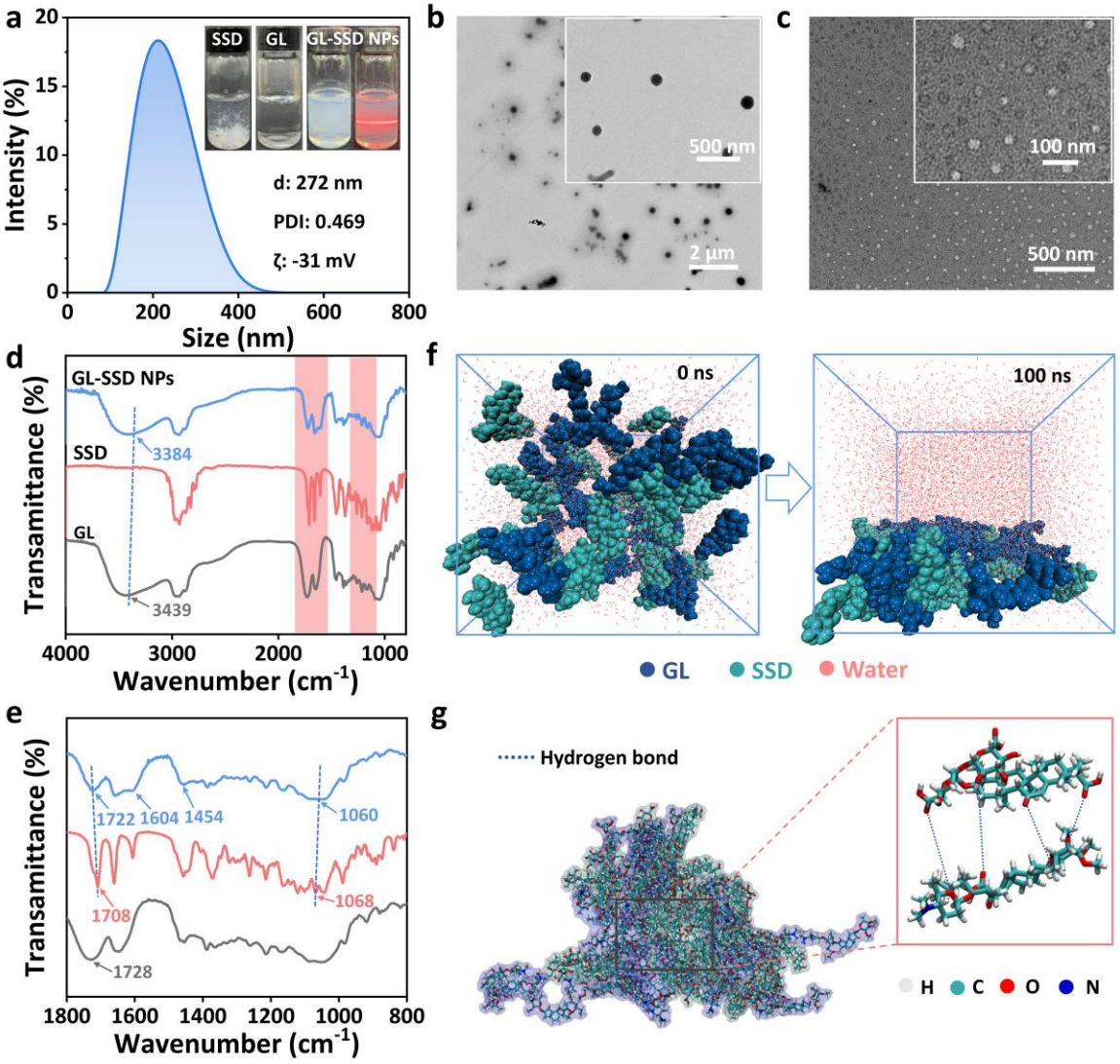

Figure 2. Co-assembly and characterization of GL-SSD NPs. a) DLS results of GL-SSD NPs. Insets: photographs of the aqueous solutions of SSD, GL, and GL-SSD NPs, as well as the Tyndall effect of GL-SSD NPs. TEM images of the morphologies of b) GL-SSD NPs and c) GL. d) FTIR spectra of GL, SSD, and GL-SSD NPs from 4000 to 800 cm^{-1}, and e) the enlarged spectra from 1800 to 800 cm^{-1}. f) Structural variations of GL and SSD during MD simulation, and g) their final intermolecular interaction patterns.

2.3 Impact behavior of GL-SSD NPs droplet on hydrophobic surfaces

The impact process of water, spinosad suspension (SSD SC), and GL-SSD NPs droplet on the surface of polytetrafluoroethylene (PTFE) film were studied using a high-speed camera. The PTFE film characterized by rough structures showed a static water contact angle of 137° (Figure S7, Supporting Information). The diameter of all impact droplets was regulated to 2.5

mm, while the release height maintained at 15 cm. As depicted in **Figure 3**a and Video S2 (Supporting Information), the maximum spreading diameter (D_{max}) of all droplets was accomplished at 2.4 ms, accompanied by the formation of anomalous contact lines by reason of rough surface and high impact velocity. For droplets of water and 0.05 wt% SSD SC, they splashed and entirely rebounded off the surface within 20 ms. On the contrary, the retraction processes of GL-SSD NPs droplets demonstrated the following behaviors: 1) for GL-SSD NPs droplet at 0.0018 wt%, the impact process was analogous to that of water, which fully rebounded at 18 ms; 2) when the concentration of GL-SSD NPs increased to 0.0088 and 0.018 wt%, the rebound of droplets was effectively suppressed with the existence of partial breaking; 3) for more concentrated GL-SSD NPs droplets (0.025, 0.030, and 0.035 wt%), no droplet splashing and bouncing occurred, and their deposition areas continuously expanded.

To better assay the droplet impact dynamic, the time evolution of the normalized spreading diameter D_t/D_0 and rebound height H_t/D_0 were summarized, where D_0, D_t, and H_t represented the initial diameter of droplet, the spread diameter of droplet, and the vertical distance from the surface to the apex of the droplet, respectively. As shown in Figure 3b, the D_t/D_0 values of all droplets ascended fleetly until reaching the maximum spreading diameter (D_{max}) at 2.4 ms, and then reduced because of the droplet retraction, where the retraction time and ultimate states were quite different. After 2.4 ms, the D_t/D_0 value of water, 0.05 wt% SSD SC, and 0.0018 wt% GL-SSD NPs droplets contiguously dwindled to 0 within 20 ms, indicating the absolute detachment of droplets from the PTFE surface. For droplets containing 0.0088 wt% and 0.018 wt% GL-SSD NPs, the equilibrium values of D_t/D_0 were 0.68 and 1.61, implying no bouncing took place. For totally deposited droplets of GL-SSD NPs at 0.025 wt%, 0.030 wt%, and 0.035 wt%, the droplets just marginally recoiled and their final equilibrium values of D_t/D_0 were 2.38, 2.33, and 2.38, respectively. Similarly, by reason of the retraction kinetic energy, the H_t/D_0 values of water, 0.05 wt% SSD SC, and 0.0018 wt% GL-SSD NPs droplets were 2.08, 1.85, and 2.2, respectively, markedly higher than those of droplets containing 0.025, 0.030, and 0.035 wt% GL-SSD NPs (Figure 3c). Given above results, the presence of GL-SSD NPs effectively suppressed the bouncing and splashing of droplets on hydrophobic surface.

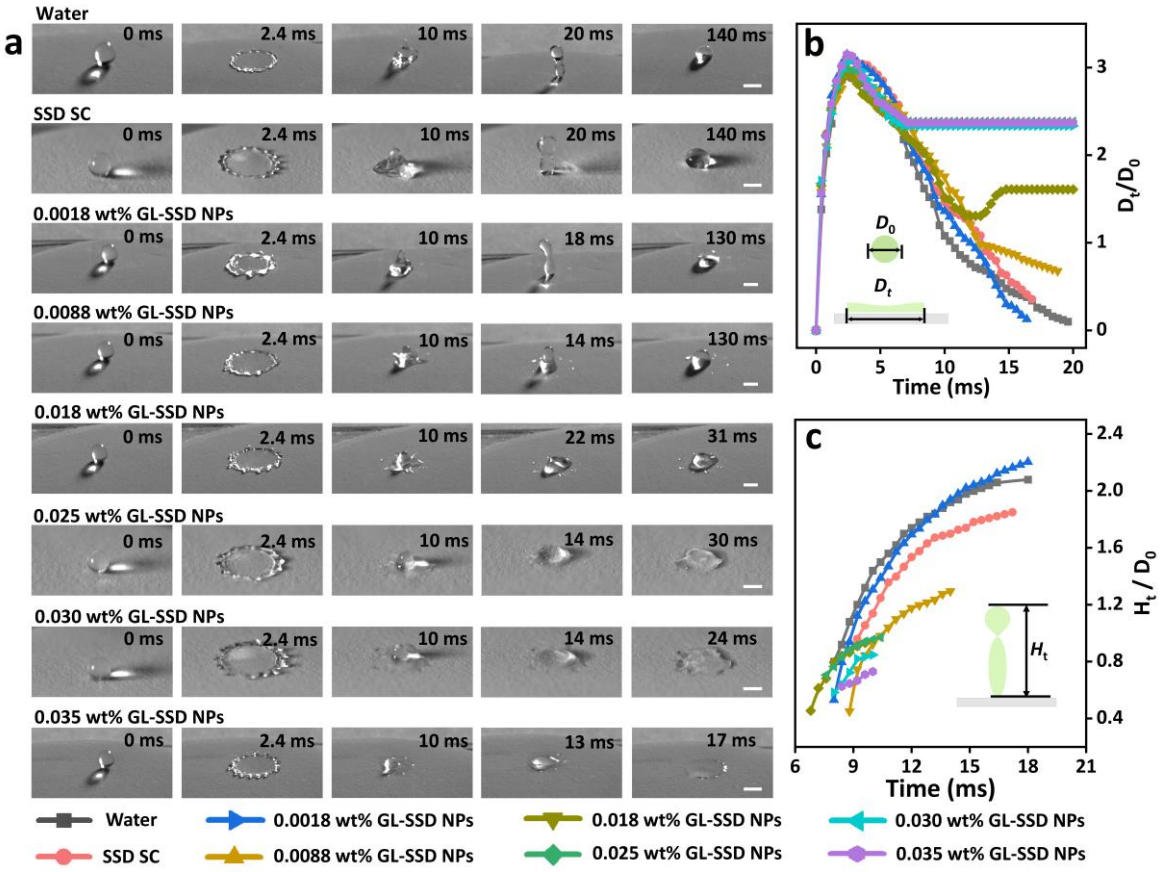

Figure 3 Impact behavior of GL-SSD NPs droplet on hydrophobic surfaces. a) Snapshots of droplet impact process on PTFE surface, including water, SSD SC, and GL-SSD NPs (0.0018, 0.0088, 0.018, 0.025, 0.030, and 0.035 wt%) droplets. Scale bar is 2 mm. All droplets were released from a vertical distance of 15 cm. Normalized b) spreading diameter (D_t/D_0) and c) rebound height (H_t/D_0) as a function of time.

2.4 Deposition mechanism of GL-SSD NPs droplets on hydrophobic surfaces

To study the mechanism of GL-SSD NPs inhibiting droplet bounce, the dynamic surface tension (DST) and viscosity of GL-SSD NPs solutions were measured. DST results showed a mild alteration of GL-SSD NPs solution within the first 100 ms, meaning a tardy diffusion rate for GL-SSD NPs (**Figure 4**a). That is to say, GL-SSD NPs were incapable of expeditiously translocating from bulk phase to interface within this short contact period between droplet and solid surface to reduce surface tension. Moreover, GL-SSD NPs solutions with different concentrations had a similar viscosity of ~1.25 mPa.s, which was comparable to that of pure water (Table S2, Supporting Information), suggesting that the

inhibited droplet rebound was independent of the dissipation of initial kinetic energy by viscosity.

Except for the properties of GL-SSD NPs droplets, the solid-liquid interaction was another crucial factor influencing the impact process of droplets. Beforehand, the equilibrium surface tension (EST) of GL-SSD NPs solutions was tested. As shown in Figure 4b, the EST value decreased to 45 mN/m as the increasing concentration from 0 to 0.018 wt%, while maintained constant after the concentration higher than 0.018 wt%. Thus, 0.018 wt% was regarded as the critical micelle concentration (CMC) of GL-SSD NPs. This was in agreement with the result in Figure 3, where the effective inhibition of droplet rebound occurred only above the concentration of 0.018 wt%. To explore the solid-liquid interactions, the dynamic adhesion behavior between GL-SSD NPs droplets (0.035 wt%, higher than CMC) and PTFE surface was studied by a high-sensitive microbalance. The sequential process of approach, contact, elongation, deformation, and separation was evidently observed in Figure 4c. After detached from PTFE surface, the water droplet was thoroughly eliminated from the surface without leaving any residue, whereas SSD SC and GL-SSD NPs droplets experienced significant elongation and break in the middle, with reserving a substantial amount of liquid on the surface. The relevant break-up distance and residual weight were analyzed in Figure 4d and 4e. The residual weights for water, SSD SC, and GL-SSD NPs were 0.35, 6.9, and 6.8 mg, respectively, while the break-up distance of GL-SSD NPs solution was 2.43 mm, much higher than 0.97 mm for water and 1.68 mm for SSD SC. It demonstrated the strongest interactions between GL-SSD NPs and PTFE surface. In addition, scanning electron microscopy (SEM) images revealed that massive droplet residues were left in the retraction trajectory after impact (Figure 4f and 4g). It was proposed that during droplet impact process the deposition of abundant GL-SSD NPs at the triple line would alter the wettability of PTFE surface by virtue of its inherent hydrophilicity, generating pinning points and delaying droplet retraction (Figure 4h).

After mastering the deposition mechanism, the bouncing behavior of water, SSD SC, and GL-SSD NPs on 30°- and 60°-tilted PTFE substrates were investigated. As shown in Figure S8 and Movie S3 (Supporting information), upon impacting water droplets were effortlessly

expelled from the surface without leaving any residue when the tilted angle was 30° and 60°, while SSD SC droplets adhered to the inclined surface at a tilted angle of 30° and rolled off completely at a tilted angle of 60°. Conversely, GL-SSD NPs droplets hardly retracted and completely deposited on the 30°-inclined surface. Even the tilted angle was 60°, a substantial amount of liquid adhering to the inclined surface was still observed. All these results further indicated that GL-SSD NPs exhibited good affinity to hydrophobic surfaces even on the inclined surface. Furthermore, in terms of the leaf characteristics and the actual application scenario of pesticides, cabbage leaf was selected as a representative hydrophobic surface for better evaluating the efficacy of GL-SSD NPs. Cabbage leaf had a micron/nano hierarchical structure and robust epicuticular wax layer, and its water contact angle was gauged to be 147°, indicating that its surface was rough and hydrophobic (Figure S9, Supporting Information). During the cultivation and maturation stages of cabbage, it is highly susceptible to the pernicious intrusion of cabbage *P. xylostella*, which seriously affects its yield and quality. While SSD is widely used in the control of cabbage *P. xylostella*, as it is a macrolide biorational pesticide with low toxicity, high efficiency, and broad spectrum. During the impact process, the droplets of water and 0.05 wt% SSD SC were rapidly retracted after reaching their maximum spread at 2.4 ms, followed by apparent splashing and complete rebound at 20 ms. On the contrary, the droplets of 0.035 wt% GL-SSD NPs adhered to the surface of cabbage leaves without breaking and splashing behavior (Figure S10, Supporting Information). Moreover, the deposition of active ingredients on cabbage leaves was evaluated by the leaf retention of water, SSD SC, and GL-SSD NPs. As shown in Figure S11 (Supporting Information), the leaf retention exhibited by GL-SSD NPs (8.15 mg/cm^2) surpassed that of both commercial SSD SC (7.01 mg/cm^2) and water (3.73 mg/cm^2). This was attributed to the abundant hydroxyl and carboxyl functional groups on GL-SSD NPs that formed hydrogen bonds with fatty acids, alcohols, and aldehydes on wax layer of leaves, enhancing the interaction force between GL-SSD NPs and the surface. Clearly, GL-SSD NPs presented a promising approach for water-based pesticide formulations aiming to regulate pesticide deposition during the spraying.

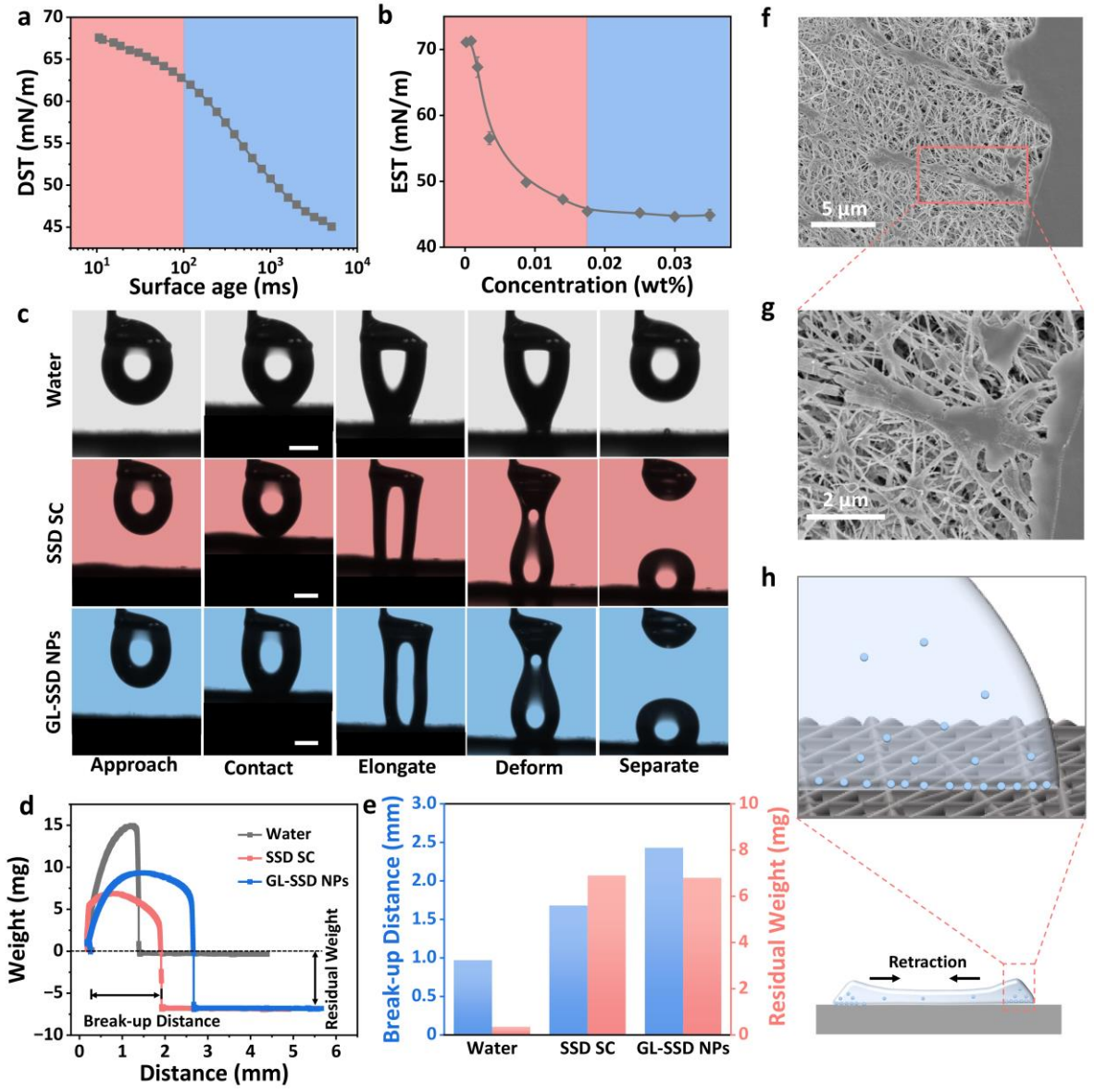

Figure 4 Deposition mechanism of GL-SSD NPs droplets on hydrophobic surfaces. a) DST of GL-SSD NPs at the concentration of 0.035 wt%. b) EST of GL-SSD NPs at varying concentrations. Error bars represented standard error (n = 3). c) Interaction process of water, SSD SC, and GL-SSD NPs with PTFE surface, including the approach, contact, elongation, deformation, and separation process. Scale bar is 1 mm. d) Weight change during the entire approach-separation process, and e) the corresponding break-up distance and residual weight of droplets on PTFE surface. f) SEM image of the residue GL-SSD NPs in the recoil route on PTFE surface after impact, and g) its partially enlarged image. h) The proposed schematic illustration of the interaction between GL-SSD NPs and PTFE surface during the droplet retraction.

2.5 Anti-photolysis, controlled-release, and bioactivity of GL-SSD NPs

The majority of pesticides like SSD are susceptible to photolysis under UV irradiation in field applications, which severely impedes their long-term control efficacy. Therefore, the anti-photolysis capability of GL-SSD NPs was comparatively investigated under UV irradiation at 254 nm. Before that, the calibration curve correlating peak area with SSD concentration was conducted (Figure S12, Supporting Information). As shown in **Figure 5**a, the degradation rate of GL-SSD NPs was dramatically lower than that of SSD SC when subjected to UV light. Approximately 100% of SSD SC degraded at 5 h, while only 63% of SSD in GL-SSD NPs was photolyzed. The half-time ($t_{1/2}$) of SSD SC and GL-SSD NPs for the pseudo-first-order kinetics were calculated to be 0.68 and 3.53 h, respectively (Table S3, Supporting Information), which meant that the protection of GL-SSD NPs against UV light was extended by 5.2 times. This may be attributed to the shielding effect of the co-assembled structure encompassing hydroxyl, carboxyl, and carbonyl groups that owned absorption capability of UV light.

The release behavior of GL-SSD NPs were investigated at different pH. As shown in Figure 5b, GL-SSD NPs showcased exceptional pH-sensitive release properties with an accelerated release rate under acidic conditions. SSD was released swiftly during the initial 24 h, and the cumulative release achieved 85%, 77%, and 62% at pH of 3, 5, and 7, respectively. After 24 h, the release rate decelerated as a result of the gradual diffusion of SSD from GL-SSD NPs into the surrounding medium. The ultimate cumulative release amount of SSD after 48 h was 96% at pH = 3 and 92% at pH = 5, higher than 75% at pH = 7. The phenomenon was caused by the protonation of carboxyl groups of GL under acidic conditions, which consequently led to a diminished electrostatic attraction with SSD and a faster release rate. Its release performance was found to be more appropriate for Weibull model in comparison with zero-order, first-order, and Higuchi model, with high correlation coefficients (R^2) of 0.969, 0.959, and 0.989 at pH levels of 3, 5, and 7, respectively (Figure 5c and S13, Supporting Information). The exponent k in Weibull model serves as an indicator of the release mechanism, where $k \leq 0.75$ follows a Fickian diffusion, $0.75 < k < 1$ conforms to a collective mechanism of Fickian diffusion and Case II transport, while $k > 1$ is attributed to complex release mechanism.[46] For

GL-SSD NPs, all *k* values were lower than 0.75 (Table S4, Supporting Information), demonstrating that its release behavior aligned with Fickian diffusion from inner to outer layers.

Insecticidal activity of GL-SSD NPs against *Plutella xylostella* was evaluated by leaf dipping method, and both SSD SC and GL-SSD NPs exposed active ingredient concentration and time dependence (Figure 5d and S14, Supporting Information). The corrected mortality of GL-SSD NPs was higher than that of SSD SC within the range of 0.625-20 mg/L. Once the exposure time extended from 24 to 48 h at a concentration of 20 mg/L, the corrected mortality rate for *P. xylostella* caused by GL-SSD NPs escalated from 87% to 100%. Moreover, the median lethal concentrations (LC_{50}) and the associated 95% confidence intervals were calculated by probit regression analysis method at 24 and 48 h to assess insecticidal activities of SSD SC and GL-SSD NPs. The LC_{50} values of GL-SSD NPs treatments at 24 and 48 h were 2.34 and 0.38 mg/L, respectively, lower than 3.87 and 0.72 mg/L of SSD SC (Figure 5e, Table S5, Supporting Information). All these results demonstrated that GL-SSD NPs had superior and sustained biological activity in comparison with SSD SC, which was ascribed to higher deposition of active ingredients on leaves. In addition, the pot experiments showed that GL-SSD NPs exhibited a conspicuous control efficacy against *P. xylostella*, and the damage degree of leaves declined with the increasing active ingredient concentration (Figure 5f). After 48 h of treatment, the leaf protection rates of GL-SSD NPs were found to be 96% and 100% at doses of 25 and 50 mg/L, respectively, higher than that of SSD SC (92%) (Figure 5g). The enhancement of control efficiency was consistent with the impact results, providing support for the notion that GL-SSD NPs can effectively improve droplet deposition on target by suppressing droplet bounce.

Given all these results, a proposed mechanism of GL-SSD NPs throughout the application process was illustrated in Figure S15 (Supporting Information), encompassing the co-assembly, efficient deposition on leaf surface, pH-controlled release, and insecticidal activity. Initially, GL and SSD stacked to form nanoparticles through electrostatic attraction, hydrogen bonding, and van der Waals force. After spraying, the GL-SSD NPs at the triple line would alter the wettability of cabbage leaf surface by virtue of its inherent hydrophilicity, which then

generated pinning points to delay the droplet retraction, leading to the enhanced deposition of droplets. Once in acidic condition, GL-SSD NPs would be dissociated to release SSD for effective control against *Plutella xylostella*. Compared with other previously reported pesticide formulations (Table S6, Supporting Information), the GL-SSD NPs is superior to most reported ones in terms of encapsulation, deposition performance, and release properties. Moreover, the co-assembly strategy avoids the use of non-renewable raw materials and tedious chemical synthesis, which has great potential for application in sustainable treatments of plant diseases.

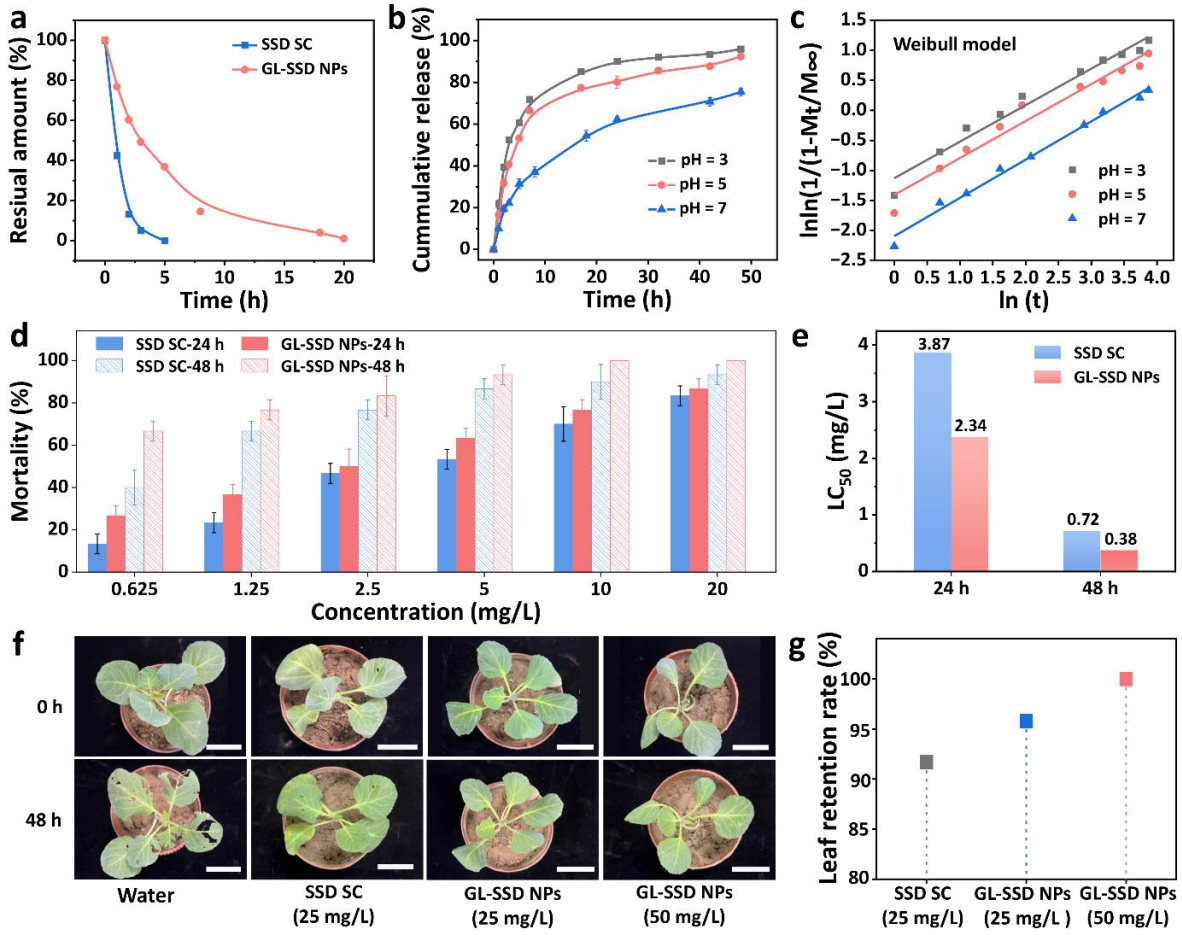

Figure 5 Anti-photolysis, controlled-release, and bioactivity of GL-SSD NPs. a) Photolysis curves of SSD SC and GL-SSD NPs under UV light at 254 nm. b) Cumulative release profiles of SSD from GL-SSD NPs at pH values of 3, 5, and 7, and c) their corresponding Weibull release models. d) Insecticidal activities of SSD SC and GL-SSD NPs against *P. xylostell* after 24 h and 48 h. e) The median lethal concentration (LC_{50}) values of SSD SC and GL-SSD NPs at 24 h and 48 h. f) Photographs of leaf damage status treated with water, SSD SC, and GL-

SSD NPs after 48 h, and g) their corresponding leaf retention rate. Scale bar in f) is 4 cm, and error bars represent standard error in (a, b, d) (n = 3). All concentrations are the active ingredient concentration in (d, e, f, j).

3. Conclusion

In summary, we have developed a supramolecular co-assembly strategy using glycyrrhizic acid (GL) and spinosad (SSD) to elaborate multi-functional and sustainable pesticide formulations. As a natural biocompatible surfactant, GL molecules can not only form an interfacial film with optimal toughness and strength at oil-water interface, but also co-assemble with SSD to afford nanoparticles. The resulting GL-SSD NPs have spherical morphologies with an average diameter of 207 nm, and possess an improved 5.2-fold photostability compared with commercial spinosad suspension (SSD SC). Upon impacting on hydrophobic surfaces of PTFE and cabbage leaf, the droplets of GL-SSD NPs exhibit strong affinity to the surface micro/nano structure, consequently inhibiting droplet rebounding and achieving an extremely higher deposition efficiency than that of water and SSD SC. In addition, the pH-controlled release of SSD is obtained because of the dynamic nature of GL-SSD NPs. Finally, indoor toxicity and pot experiments indicate that GL-SSD NPs owned good insecticidal activity against *Plutella xylostella*, even at an ultralow pesticide dosage. This work provides an alternative approach for the development of sustainable pesticide formulations featuring high deposition and controlled-release, which may have broad potentials in actual agriculture production.

4. Experimental Section

Preparation of GL-SSD NPs: Initially, GL (5 mg) was added into deionized water (10 mL) and subjected to heating at 90℃ for 30 min. After cooling to ambient temperature, a methanol solution of SSD (11 mg/mL, 200 μL) was meticulously added dropwise to above aqueous solution under ultrasonic condition for 20 min. The mixed solution was then transferred to a dialysis bag with a molecular weight cutoff of 1000 Da and dialyzed in deionized water at room temperature for 24 h to remove methanol and unassembled small molecules. Lastly, a suspension of the co-assembled GL-SSD NPs was obtained.

Statistical Analysis

All data were acquired from no fewer than three independent experiments and expressed as the mean ± standard deviation. Significant differences of multiple groups were statistically analyzed using SPSS software using one-way ANOVA followed by a Duncan test ($p < 0.05$).

Supporting Information

Supporting Information is available from the Wiley Online Library or from the author.

Acknowledgements

This work is supported by Beijing Natural Science Foundation (L233016) and the Open Fund of Anhui Province Key Laboratory of Environment-friendly Polymer Materials.

Conflict of Interest

The authors declare no conflict of interest.

Received: ((will be filled in by the editorial staff))
Revised: ((will be filled in by the editorial staff))
Published online: ((will be filled in by the editorial staff))

References

[1] M. Kah, R. S. Kookana, A. Gogos, T. D. Bucheli, *Nat. Nanotechnol.* **2018**, *13*, 677.

[2] E. Crist, C. Mora, R. Engelman, *Science* **2017**, *356*, 260.

[3] K. Koch, B. Bhushan, W. Barthlott, *Prog. Mater. Sci.* **2009**, *54*, 137.

[4] A. Gauthier, S. Symon, C. Clanet, D. Quéré, *Nat. Commun.* **2015**, *6*, 8001.

[5] B. Wang, J. Wang, C. Yu, S. Luo, J. Peng, N. Li, T. Wang, L. Jiang, Z. Dong, Y. Wang, *Glob. Chall.* **2023**, *7*, 2300007.

[6] M. Nuruzzaman, M. M. Rahman, Y. Liu, R. Naidu, *J. Agric. Food Chem.* **2016**, *64*, 1447.

[7] X. Zhao, H. Cui, Y. Wang, C. Sun, B. Cui, Z. Zeng, *J. Agric. Food Chem.* **2018**, *66*, 6504.

[8] C. Lamberth, S. Jeanmart, T. Luksch, A. Plant, *Science* **2013**, *341*, 742.

[9] C. J. Topping, A. Aldrich, P. Berny, *Science* **2020**, *367*, 360.

[10] M. Song, J. Ju, S. Luo, Y. Han, Z. Dong, Y. Wang, Z. Gu, L. Zhang, R. Hao, L. Jiang, *Sci. Adv.* **2017**, *3*, e1602188.

[11] Z. Li, Y. Ma, K. Zhao, C. Zhang, Y. Gao, F. Du, *ACS Sustainable Chem. Eng.* **2021**, *9*, 2891.

[12] V. Bergeron, D. Bonn, J. Y. Martin, L. Vovelle, *Nature* **2000**, *405*, 772.

[13] L. Chen, Y. Wang, X. Peng, Q. Zhu, K. Zhang, *Macromolecules* **2018**, *51*, 7817.

[14] M. Damak, S. R. Mahmoudi, M. N. Hyder, K. K. Varanasi, *Nat. Commun.* **2016**, *7*, 12560.

[15] L. Zhang, J. Wang, Y. Fan, Y. Wang, *Adv. Sci.* **2023**, *10*, 2300270.

[16] X. Zhao, Q. Zeng, S. Yang, F. He, W. Qin, Z. Wang, K. Mai, G. Yu, J. Huang, J. Li, Y. Feng, *Chem. Eng. J.* **2023**, *463*, 142362.

[17] Y. Meng, Z. Li, C. Xie, Y. Gao, X. Yu, H. Zhang, H. Li, J. Hu, *Cell Rep. Phys. Sci.* **2022**, *3*, 100810.

[18] X. Han, J. Li, X. Tang, W. Li, H. Zhao, L. Yang, L. Wang, *Small* **2022**, *18*, e2200277.

[19] K. Wei, K. Zhao, Y. Gao, H. Zhang, X. Yu, M. Li, J. Hu, *Chem. Eng. J,* **2023**, *462*, 142191.

[20] Y. Shen, C. An, J. Jiang, B. Huang, N. Li, C. Sun, C. Wang, S. Zhan, X. Li, F. Gao, X. Zhao, H. Cui, R. Gooneratne, Y. Wang, *ACS Nano* **2022**, *16*, 20622.

[21] D. Zhang, J. Du, R. Wang, J. Luo, T. Jing, B. Li, W. Mu, F. Liu, Y. Hou, *Adv. Funct. Mater.* **2021**, *31*, 2102027.

[22] M. Wan, T. Hong, G. He, Y. Zhao, L. Sun, *Chem. Eng. J.* **2023**, *475*, 146461.

[23] J. Dong, W. Chen, D. Qin, Y. Chen, J. Li, C. Wang, Y. Yu, J. Feng, X. Du, *J. Hazard. Mater.* **2021**, *419*, 126404.

[24] S. Song, Y. Wang, J. Xie, B. Sun, N. Zhou, H. Shen, J. Shen, *ACS Appl. Mater. Interfaces* **2019**, *11*, 34258.

[25] S. Kumar, M. Nehra, N. Dilbaghi, G. Marrazza, A. A. Hassan, K.-H. Kim, *J. Control. Release* **2019**, *294*, 131.

[26] D. Wang, N. B. Saleh, A. Byro, R. Zepp, E. Sahle-Demessie, T. P. Luxton, K. T. Ho, R. M. Burgess, M. Flury, J. C. White, C. M. Su, *Nat. Nanotechnol.* **2022**, *17*, 347.

[27] B. Liu, Y. Fan, H. Li, W. Zhao, S. Luo, H. Wang, B. Guan, Q. Li, J. Yue, Z. Dong, Y. Wang, L. Jiang, *Adv. Funct. Mater.* **2020**, *31*, 2006606.

[28] G. M. Whitesides, B. Grzybowski, *Science* **2002**, *295*, 2418.

[29] Y. Mai, Z. An, S. Liu, *Macromol. Rapid Commun.* **2022**, *43*, 2200481.

[30] L. Qiao, H. Yang, S. Gao, L. Li, X. Fu, Q. Wei, *J. Mater. Chem. B* **2022**, *10*, 1908.

[31] S. Jiwpanich, J. H. Ryu, S. Bickerton, S. Thayumanavan, *J. Am. Chem. Soc.* **2010**, *132*, 10683.

[32] A. Rao, S. Roy, V. Jain, P. P. Pillai, *ACS Appl. Mater. Interfaces* **2023**, *15*, 25248.

[33] G. Tang, Y. Tian, Y. Gao, Z. Zhou, X. Chen, Y. Li, X. Yu, H. Wang, X. Li, Y. Cao, *ACS Nano* **2022**, *16*, 4892.

[34] J. Yang, H. Ye, H. Xiang, X. Zhou, P. Wang, S. Liu, B. Yang, H. Yang, L. Liu, S. Yang, *Adv. Funct. Mater.* **2023**, *33*, 2303206.

[35] C. Zhang, X. Yang, S. Yang, Z. Liu, L. Wang, *Chem. Eng. J.* **2022**, *430*, 133011.

[36] T. Kao, C. Wu, G. Yen, *J. Agric. Food Chem.* **2014**, *62*, 542.

[37] A. Saha, J. Adamcik, S. Bolisetty, S. Handschin, R. Mezzenga, *Angew. Chem. Int. Ed.* **2015**, *54*, 5408.

[38] Z. Wan, Y. Sun, L. Ma, X. Yang, J. Guo, S. Yin, *J. Agric. Food Chem.* **2017**, *65*, 2394.

[39] Y. Qian, Y. Zheng, J. Jin, X. Wu, K. Xu, M. Dai, Q. Niu, H. Zheng, X. He, J. Shen, *Adv. Mater.* **2022**, *34*, 2200521.

[40] Y. Ma, Y. Gao, K. Zhao, H. Zhang, Z. Li, F. Du, J. Hu, *ACS Appl. Mater. Interfaces* **2020**, *12*, 50126.

[41] V. S. V. Santos, B. B. Pereira, *J. Toxicol. Env. Heal. B* **2020**, *23*, 13.

[42] G. Li, J. Wang, X. Kong, *Carbohydr. Polym.* **2020**, *249*, 116865.

[43] Y. Hata, S. Yoneda, S. Tanaka, T. Sawada, T. Serizawa, *J. Colloid Interface Sci.* **2021**, *590*, 487.

[44] S. Sun, Y. Luo, Y. Yang, J. Chen, S. Li, Z. Wu, S. Shi, *Small* **2022**, *18*, 2204182.

[45] W. Pi, L. Wu, J. Lu, X. Lin, X. Huang, Z. Wang, Z. Yuan, H. Qiu, J. Zhang, H. Lei, P. Wang, *Bioact. Mater.* **2023**, *29*, 98.

[46] V. Papadopoulou, K. Kosmidis, M. Vlachou, P. Macheras, *Int. J. Pharm.* **2006**, *309*, 44.